applied sciences

MDPI

Article

Analysis of the Slanted-Edge Measurement Method for the Modulation Transfer Function of Remote Sensing Cameras

Jian Yu [1,2], Yu Zhang [1,*], Biao Qi [1], Xiaotian Bai [1,2], Wei Wu [1,2] and Hongxing Liu [1]

[1] Changchun Institute of Optics, Fine Mechanics and Physics, Chinese Academy of Sciences, Changchun 130033, China
[2] University of Chinese Academy of Sciences, Beijing 100049, China
* Correspondence: zhangyu@ciomp.ac.cn

Abstract: The modulation transfer function (MTF) serves as a crucial technical index for assessing the imaging quality of remote sensing cameras, which is integral throughout their entire operational cycle. Currently, the MTF evaluation of remote sensing cameras primarily relies on the slanted-edge method. The factors influencing the slanted-edge method's effectiveness are broadly classified into two categories: algorithmic factors and image factors. This paper innovatively comprehensively analyzes the influencing factors of the slanted-edge method and proposes an improved slanted-edge method to calculate the MTF testing method of remote sensing cameras, which is applied to the MTF testing of remote sensing cameras. Since the traditional algorithm can only be applied in the small angle situation, this paper proposes a new method of slanted-edge method test calculation based on the optimal oversampling rate (OSR) adaptive model of the slanted edge and uses simulation experiments to verify the reliability of the algorithm model through the deviation of the slanted-edge angle calculation and MTF measurement, and the results show that the algorithm improves the accuracy of the MTF measurement compared with the ISO-cos and OMINI-sine methods. Then, the effects of the slanted-edge angle, image region of interest (ROI), as well as image contrast and signal-to-noise ratio (SNR) on the accuracy of the MTF calculation by the slanted-edge method were quantitatively analyzed as the constraints of the slanted-edge method test. Based on the laboratory target experiment, the algorithm flow and various influencing factors obtained in the simulation stage are verified, and the experimental results are more consistent with the various test results obtained in the simulation stage. Consequently, the slanted-edge method introduced in this paper is applicable for future remote sensing camera MTF testing. This approach offers a valuable reference for on-orbit focusing, satellite operational condition monitoring, lifespan estimation, and image restoration.

Keywords: remote sensing camera; MTF; slanted-edge method; accuracy analysis; influencing factors

Citation: Yu, J.; Zhang, Y.; Qi, B.; Bai, X.; Wu, W.; Liu, H. Analysis of the Slanted-Edge Measurement Method for the Modulation Transfer Function of Remote Sensing Cameras. *Appl. Sci.* **2023**, *13*, 13191. https://doi.org/10.3390/app132413191

Academic Editor: Mihailo Ristic

Received: 19 November 2023
Revised: 4 December 2023
Accepted: 8 December 2023
Published: 12 December 2023

1. Introduction

In the lifecycle of remote sensing cameras, from system installation and long-distance transportation to launch impact and in-orbit operation, various factors such as the space environment and component aging lead to a gradual decline in imaging system performance [1]. This deterioration results in diminished image quality and information content. High-quality space images are crucial for delivering accurate and comprehensive data, necessitating regular in-orbit quality assessments of remote sensing cameras to monitor performance shifts. The MTF is a critical parameter for evaluating the imaging quality of optical systems [2]. It quantifies the extent of information attenuation during object imaging, offering higher accuracy and a more objective and comprehensive assessment than traditional methods. As an ideal performance index for orbiting remote sensing cameras, MTF measurements are also vital for predicting the lifespan of satellite imaging systems [3], assisting in satellite in-orbit adjustments, and facilitating image recovery and reconstruction.

MTF detection methods vary depending on the target used, including the three-bar method [4], slanted-edge method [5], slit method [6], and Siemens Star method [7,8]. Currently, laboratory testing of camera MTF predominantly employs the three-bar and slanted-edge methods, as other methods face limitations due to challenges in target processing, extended testing durations, and poor repeatability, leading to less frequent application. The slanted-edge method, a primary technique for remote sensing camera MTF detection [9], involves rotating a slanted-edge target at a specific angle relative to the detector's rows or columns. This rotation projects and rearranges the pixels of the slanted-edge image based on a predefined rule [10], thereby enhancing the image's sampling rate and mitigating under-sampling issues. Recognized as an indirect approach for measuring the MTF, the slanted-edge method has been successfully implemented in the in-orbit MTF measurement of satellites such as IKONOS [11,12], Orbview [13], GF-4 [14], and Quickbird [15]. The International Organization of Standards endorses this method as well (ISO12233:2023) [16], which involves analyzing a camera-captured slanted-edge target image to determine the edge spread function (ESF) [17], differentiating the ESF to acquire the line spread function (LSF), and then applying Fourier transform on the LSF and taking the modes to compute the MTF [18,19]. Offering a comprehensive evaluation at various spatial frequencies in a single instance and characterized by rapid detection, the slanted-edge method has garnered significant scholarly interest [20].

The accuracy of the slanted-edge method hinges on precise estimation of the image edge angle, as this directly impacts the MTF calculation results. Masaoka et al.'s [21] approach utilizes the Sobel operator and the Hough transform for edge angle estimation, examining how estimation errors affect the method's accuracy. Roland [22] focused on the impact of inclination estimation errors on the stability and repeatability of MTFs obtained via this method. A critical step in the slanted-edge method's algorithm involves differentiating the ESF to derive the LSF, a process that can amplify noise. Consequently, noise impact analysis and suppression techniques have become a focal area of research. To mitigate noise's impact on accuracy, scholars have suggested fitting the ESF with a function model. Tzannes and Mooney [23] and J. M. Mooney, for instance, identified the midpoint of each data row as half the mean gray value between the dark and light regions of the slanted-edge image, constructing an oversampled ESF fitted with a Fermi function to counter noise effects. Hwang et al. [24] enhanced MTF detection accuracy by refining the ISO 12233 slanted-edge method with a similar Fermi function fitting of the ESF, while Masaoka [25] achieved higher accuracy through an oversampling ESF, employing image rotation, cumulative distribution function fitting, and projection.

The analysis above reveals that the MTF testing of remote sensing cameras using the slanted-edge method is significantly influenced by the chosen calculation method, with varying algorithmic models leading to considerable deviations in results [26]. In this paper, according to the working state of the space camera on orbit and the imaging characteristics, combined with the relevant theories of optoelectronic imaging systems, the optimal algorithm based on the slanted-edge optimal OSR adaptive model's slanted-edge method calculation is proposed through the study of the sub-pixel edge detection fitting algorithm and edge diffusion function extraction. The GLCM method is used to detect the sub-pixel edges and accurately locate the edge position, and then the edge points are projected, and the sub-pixel arrays are sampled, fitted, and smoothed with a variable OSR for different angles to obtain the ESF, and the differentiation of the ESF curves is used to obtain the LSF, and the smoothing of the LSF curves is performed by using the Tukey window function. Finally, the Fourier transform mode normalization is applied to the LSF curve to obtain the MTF curve. In order to verify the reasonableness of the algorithm, simulation experiments are used to verify the response of the imaging system to the spatial frequency through the mathematical function to simulate the response of the imaging system to the spatial frequency and obtain the slanted-edge image and the theoretical MTF curve, respectively, using the ISO-cos, OMNI-sine, and the algorithm proposed in this paper to calculate the MTF curve of the slanted-edge image and compare it with the

theoretical MTF curve, which shows that the MTF curve of the proposed algorithm at each frequency has a higher similarity to the theoretical MTF curve, verifying the reasonableness of the algorithm in this paper. This study shows that the MTF curves at each frequency of the proposed algorithm have high similarity with the theoretical MTF curves, which verifies the reasonableness of the algorithm in this paper.

Subsequently, the image factors affecting the calculation of the slanted-edge method are analyzed. It establishes the relationship between the slanted-edge angle and ROI in the MTF calculation results through simulation. The simulation results are then compared in terms of accuracy and stability to ascertain the optimal slanted-edge angle range and the ideal ROI range for the slanted-edge method. Under optimal conditions for the slanted-edge angle and image ROI, simulations are conducted to obtain images with varying contrasts and SNRs. These simulations aim to investigate the impact of these varying contrasts and SNRs on the calculation results. In the laboratory, the MTF test validation system was constructed. This system utilized a customized slanted-edge target to capture test images via the optical system imaging process. Subsequently, the MTF test was conducted to validate the efficacy of the slanted-edge test method proposed in this paper.

The rest of this paper is structured as follows: In Section 2, the foundational concept of the MTF and the procedural aspects of MTF calculation through the slanted-edge method are introduced. This section also delves into the analysis of algorithmic factors affecting the results of the slanted-edge method, presenting processing steps of the algorithm based on a slanted-edge optimal OSR adaptive model. Section 3 scrutinizes the impact of image factors on the results of the slanted-edge method calculation and proposes constraints for this calculation method. Section 4 presents and analyzes the results of the experiments conducted. Finally, Section 5 offers a comprehensive summary of the entire paper and outlines directions for future research.

2. Measurement Principles and Methods

Per the principles of Fourier optical imaging, in a specific imaging system, when an ideal point light source serves as the input function, the resulting output is not a concentrated point but rather a distinct spot [27]. This phenomenon is known as the point spread function (PSF) [28], exemplified in Figure 1.

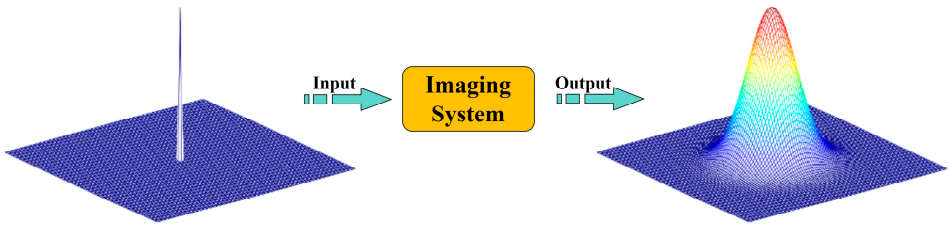

Figure 1. Formation of point spread function.

The PSF characterizes the response of an imaging system to an ideal point source, illustrating the diffusion of this source on the imaging plane and thereby unveiling the system's spatial resolution. The optical transfer function (OTF) [29,30], as delineated in Equation (1), emerges from the two-dimensional Fourier transform of the PSF [10]. It embodies the imaging system's response to various spatial frequencies and is composed of two components: the amplitude and the phase parts.

$$OTF(u,v) = \mathcal{F}\{PSF(x,y)\} \tag{1}$$

Here, $\mathcal{F}$ is the Fourier transform, x, y are the spatial coordinates, and u, v are the frequency coordinates.

The OTF provides a comprehensive description of an imaging system's capacity to transfer spatial details, encompassing both contrast and phase information [31]. The MTF, constituting the magnitude component of the OTF, specifically reflects the system's

proficiency in transferring contrast across various spatial frequencies. Accordingly, the MTF is formulized as shown in Equation (2):

$$MTF(u,v) = |OTF(u,v)| \tag{2}$$

Similarly, the LSF is the light intensity distribution captured on the image plane after imaging of a line source, either $\delta(x)$ or $\delta(y)$. The LSF is essentially the integral of the PSF along a specified direction, and its one-dimensional Fourier transform provides the cross-section profile of the MTF in that direction, as demonstrated in Equation (3):

$$\begin{aligned} LSF_x(x) &= \int PSF(x,y)dy \\ LSF_y(y) &= \int PSF(x,y)dx \end{aligned} \tag{3}$$

When the input function is a step function, typically exemplified by the slanted-edge image region of a remote sensing image, its resultant output function is the ESF. This output represents the two-dimensional light intensity distribution post-optical system processing. The ESF can be viewed as the integral of the LSF, establishing a relationship between differentiation and integration, as illustrated in Equation (4). Furthermore, the one-dimensional Fourier transform of the LSF corresponds to the MTF for that specific direction [32], forming the theoretical foundation of the slanted-edge method used in MTF calculation.

$$\begin{aligned} ESF(x) &= \int_{-\infty}^{x} LSF(x')dx' \\ LSF(x) &= \frac{d}{dx}ESF(x) \end{aligned} \tag{4}$$

As delineated by the aforementioned theory, the interrelationship among PSF, LSF, ESF, and MTF is depicted in Figure 2. Consequently, by acquiring any one of LSF, PSF, or ESF, the MTF can be derived based on this established relationship [33,34].

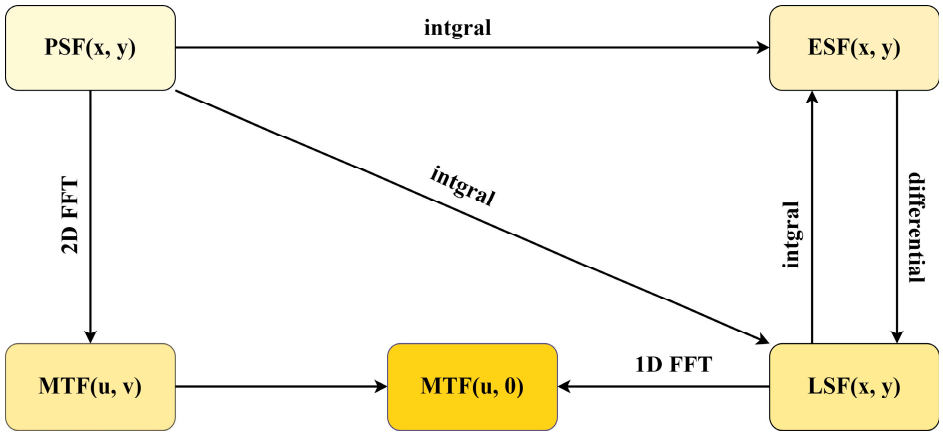

Figure 2. Relationship between PSF, ESF, LSF, and MTF.

The principal procedures for computing the MTF using the slanted-edge method [14], as applied in remote sensing imagery, are illustrated in Figure 3:

(1) Identify and capture an image of the slanted-edge calculation region in the remote sensing image, ensuring it conforms to specific criteria; the edge should be straight and form a slight angle with the detector's image element direction.
(2) Conduct image preprocessing on the slanted-edge region to minimize random noise, followed by sub-pixel slanted-edge detection to ascertain the sub-pixel location of the slanted edge.
(3) Gather data points adjacent to the slanted edge and perform multi-line alignment using the precise sub-pixel slanted-edge positions from step 2, resulting in the ESF of densely sampled points.

(4) Compute the derivative of the ESF to generate the LSF curve.
(5) Apply the Fourier transform to the LSF, yielding the MTF curve.

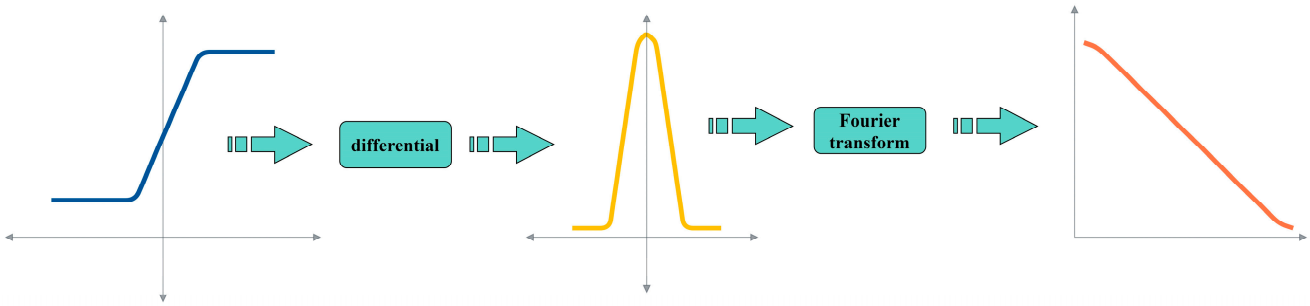

Figure 3. Schematic calculation of slanted-edge method.

2.1. Sub-Pixel Edge Detection and Fitting

The sub-pixel edge detection step is pivotal in the slanted-edge method, as accurate determination of the sub-pixel edge position is essential for proper alignment and fitting in subsequent stages. Presently, sub-pixel edge detection techniques can be broadly classified into three categories: moment-based, interpolation-based, and edge model function fitting-based approaches. In this paper, we employ one method from each category for sub-pixel edge detection using the slanted-edge method: gray-level co-occurrence matrix (GLCM) [35], bilinear interpolation (BLI) [36], and hyperbolic tangent fitting (HTF) [37]. Since sub-pixel edge detection is executed for each row of data points, the methods used are inherently one-dimensional. We simulate, compare, and analyze the accuracy and influencing factors of these methods to identify the most effective sub-pixel edge detection technique for the slanted-edge method.

2.1.1. Gray-Level Co-Occurrence Matrix (GLCM) Method

The GLCM sub-pixel edge detection method operates on the principle of invariant GLCM, comparing the actual edge with an ideal edge model to accurately localize the image edge. This method presupposes that the one-dimensional ideal edge model resembles a step function, $u(x)$, with gray values g_1 and g_2 on either side of the edge and a step height of h. The ideal edge configuration is therefore represented as follows:

$$E(x) = (g_1 - g_2) \times u(x - h) + g_1 \tag{5}$$

where ω_1, ω_2 are the proportions of pixel points with gray values g_1, g_2, respectively, relative to the total number of pixel points in the entire edge region, adhering to the equation: $\omega_1 + \omega_2 = 1$. Assuming x_j represents the GLCM value at an edge point, we consider the first three moments of this value.

$$\overline{m} = \sum_{j=1}^{2} \omega_j g_j^i = \frac{1}{n} \sum_{j=1}^{n} x_j^i \tag{6}$$

Here, n is the total number of pixel points, with the actual edge density denoted as $\omega = k/n$. This value of ω can be deduced through calculation as follows:

$$\begin{gathered} \omega_1 = 0.5\left[1 + \bar{s}\sqrt{1/\left(4 + \bar{s}^2\right)}\right] g_1 = \overline{m_1} - \overline{\sigma}\sqrt{\frac{\omega_2}{\omega_1}}, g_2 = \overline{m_2} - \overline{m_1} \\ \bar{s} = \frac{1}{n}\sum_{i=1}^{n} \frac{(x_i - \overline{m_1})^3}{\sigma^3} = \frac{\overline{m_1} + 2\overline{m_1}^3 - 3\overline{m_1}\,\overline{m_2}}{\sigma^3} \end{gathered} \tag{7}$$

Consequently, the edge position in the actual image is determined as follows:

$$k = np_1 - \frac{1}{2} = \frac{n}{2}\sqrt{\frac{s}{4 + \bar{s}^2}} + (n-1)/2 \tag{8}$$

2.1.2. Bilinear Interpolation (BLI) Method

Bilinear interpolation, an advancement of linear interpolation in two dimensions, facilitates the estimation of pixel values at undefined points within an image. This method approximates the value of a new pixel point by utilizing the values of its four neighboring pixels. It is particularly effective for tasks like image scaling, rotation, and sub-pixel edge detection [38].

Consider a pixel point with a sub-pixel location designated as (x, y). To employ bilinear interpolation, it is necessary to identify the four nearest integer pixel locations surrounding this point. Typically, these locations are represented as (x_1, y_1), (x_1, y_2), (x_2, y_1), (x_2, y_2), where x_1, x_2 are the nearest integers to x, obtained by rounding down and up, respectively, and similarly for y_1, y_2 with respect to y.

Initially, linear interpolation is conducted in the x-direction, which entails calculating the values at points (x, y_1) and (x, y_2).

$$\begin{aligned} f(x, y_1) &= f(x_1, y_1) + (x - x_1) \cdot (f(x_2, y_1) - f(x_1, y_1)) \\ f(x, y_2) &= f(x_1, y_2) + (x - x_1) \cdot (f(x_2, y_2) - f(x_1, y_2)) \end{aligned} \tag{9}$$

A linear interpolation is then conducted in the direction where the values of (x, y_1) and (x, y_2) have already been calculated.

$$f(x, y) = f(x, y_1) + (y - y_1) \cdot (f(x, y_2) - f(x, y_1)) \tag{10}$$

The interpolation results from the two aforementioned directions are combined to derive the final interpolation expression, incorporating the respective weights of these two directions:

$$\begin{aligned} f(x, y) = (1 - t)(1 - u) f(x_1, y_1) + t(1 - u) f(x_2, y_1) \\ + (1 - t) u f(x_1, y_2) + t u f(x_2, y_2) \end{aligned} \tag{11}$$

where t, u represent the differences in distances along the x-axis and y-axis, respectively, defined as $t = x - x_1$ and $u = y - y_1$, where x_1, y_1 correspond to the coordinates of the lower left pixel point.

2.1.3. Hyperbolic Tangent Fitting (HTF) Method

Angela Cantatore et al. proposed the hyperbolic tangent fitting method as an edge model. This approach aligns the actual edge gray-level distribution with the model to enhance sub-pixel edge detection accuracy. The hyperbolic tangent function, an S-type function, is generally expressed as follows:

$$f(x) = A \cdot \tanh(B(x - C)) + D \tag{12}$$

where A is the curve's magnitude, B is the slope, C is the curve's center position (i.e., the edge position), and D is the offset.

In sub-pixel edge detection, a set of grayscale values $I(x)$ from edge pixels is analyzed, where x indicates the pixel position. The objective is to determine the optimal values of A, B, C, and D that best fit these data. Initially, a rough edge location is identified using initial edge detection, and the surrounding gray values are extracted. Subsequently, a fitting window encompassing a series of pixel points near the edge is chosen in the vicinity of this initial edge location. The method employs least squares to determine the optimal parameters A, B, C, and D, thereby minimizing the discrepancy between the fitted function $f(x)$ and the actual gray value $I(x)$. This is accomplished by addressing the following optimization problem:

$$\min_{A,B,C,D} \sum_{x} [I(x) - (A \cdot \tanh(B(x - C)) + D)]^2 \tag{13}$$

The optimization problem can be solved using a nonlinear least-squares algorithm, and in this paper the Levenberg–Marquardt algorithm is used to solve it.

2.1.4. Simulation Experiment

This comparative analysis evaluates the three methods discussed above through simulation. Firstly, a slanted-edge image, measuring 30 pixels in both length and width, is selected. The results of applying these three sub-pixel edge detection methods are illustrated in Figure 4.

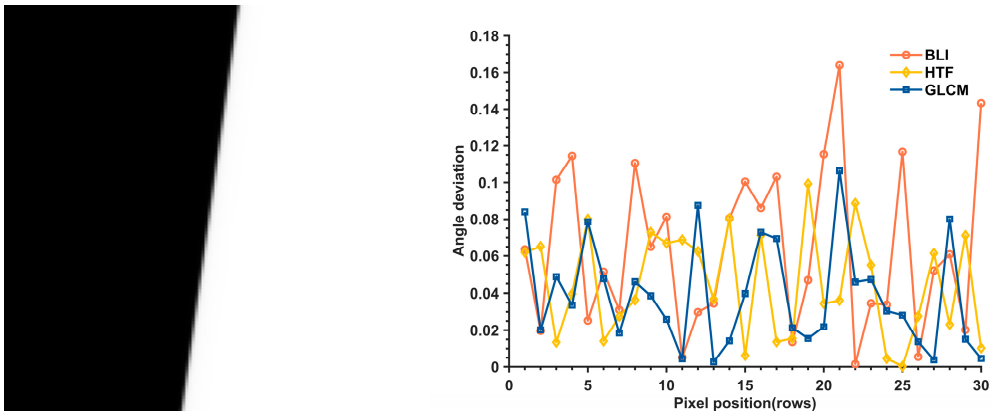

(**a**) (**b**)

Figure 4. The calculated results for three sub-pixel edge detection methods are as follows: (**a**) the slanted-edge image; (**b**) the deviation between the calculated and theoretical edge positions.

Without considering random noise, Table 1 shows that all three sub-pixel edge detection accuracies are high, with the interpolation method having an error of less than 0.06 pixels, while the GLCM and fitted methods have significantly higher accuracies than the interpolation method, with an error of less than 0.03 pixels.

Table 1. Mean and standard deviation of sub-pixel edge deviations calculated by the three methods.

Indicator \ Method	GLCM	BLI	HTF
Angle deviation MEAN	0.063718	0.044824	0.038874
Angle deviation SD	0.043189	0.02798	0.028086

Gaussian noise, with a noise standard deviation ranging from 0.001 to 0.010 in increments of 0.001, was added to the simulated image for blurring purposes. Subsequently, the root-mean-square error (RMSE) between the measured and theoretical values of the GLCM, BLI, and HTF detection methods was calculated under varying noise conditions. The results of these calculations are depicted in Figure 5.

The introduction of varying levels of Gaussian noise reduces the accuracy of the three methods under consideration. Specifically, the accuracy of the BLI method is significantly compromised by random noise, with edge detection errors escalating rapidly from 0.06 pixels to 0.7 pixels post-noise addition. Conversely, the GLCM and HTF methods exhibit more resilience to random noise, with errors incrementally rising to only 0.1 pixels. Notably, the GLCM method demonstrates commendable accuracy, comparable to the fitting method. However, its shorter processing time makes it particularly suited to real-time detection requirements. Consequently, this paper opts for the GLCM method, balancing accuracy with operational efficiency.

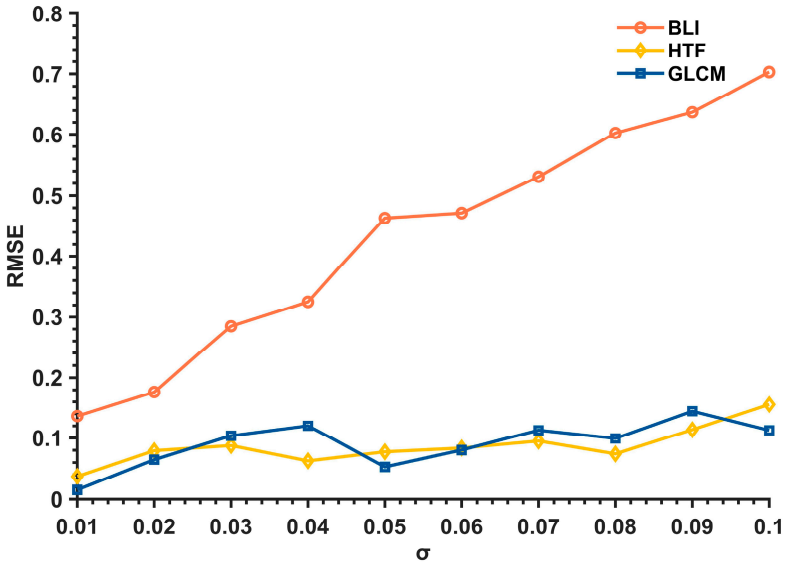

Figure 5. RMSE of three methods for detecting edges under different noise conditions.

2.2. ESF Processing Methods

Extracting the ESF curve is a crucial step in ensuring the computational accuracy of the slanted-edge method. The optical imaging system's conversion of optical signals into electrical signals on the detector results in a down-sampling phenomenon [39]. This varies based on pixel size and leads to the edge image data manifesting as a discrete sequence of points rather than a continuous curve. Consequently, part of the ESF curve information is missing, which directly impacts the accuracy of the MTF. To address this issue, a multi-line edge alignment method is employed to create a more densely sampled ESF curve.

Firstly, the pixels within the edge image's ROI are projected. This projection can be executed in two ways: horizontally or perpendicular to the slanted edge, as illustrated in Figure 6. While these projection methods yield similar results when the edge angle is small, they diverge significantly as the edge angle increases.

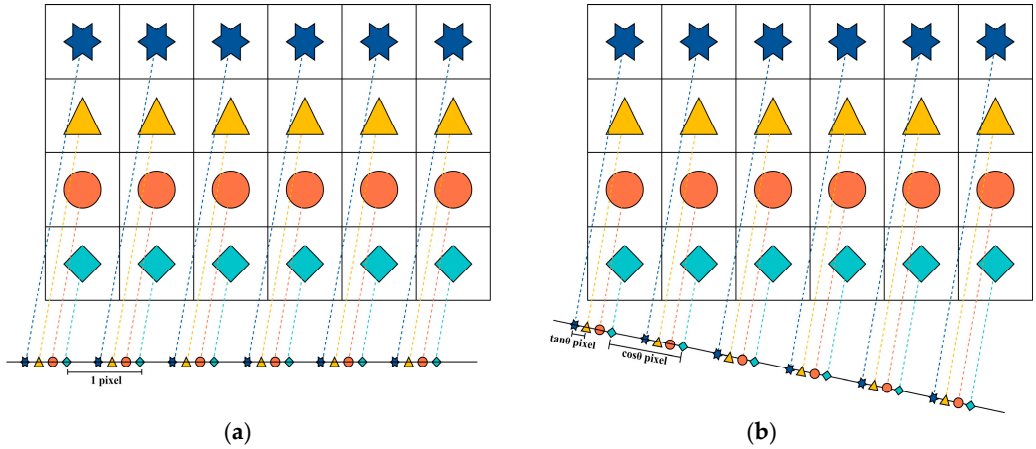

Figure 6. Comparison of different projection methods: (**a**) horizontal direction; (**b**) vertical slanted-edge direction.

In this paper, the ROI image is projected orthogonally to its edge. The subsequent one-dimensional (1D) pixel array requires sub-pixel oversampling, where the bin width is a critical parameter. In the methods outlined in ISO 12233, ISO-cos, and OMNI, a 4x OSR is utilized. The primary distinction among these methods lies in the variation in bin width relative to the edge's inclination angle. Specifically, ISO 12233 and OMNI employ a constant bin width of 1/4 pixel, independent of the angle, whereas ISO-cos adjusts the width based

on the neighboring pixel dimensions at the projection level, resulting in a bin width of $(\cos\theta)/4$ pixel. At any edge angle, when $\tan\theta = 1/4$, the ISO-cos method aligns the edge image's pixel projection intervals with the oversampling bin width. However, for angles exceeding 14.04°, where the projection interval of each pixel column fails to align with the bin width, resulting in a gap larger than the bin width, the assumptions about the random phases of the imaging system's sampling points are violated. This misalignment leads to inaccuracies in the MTF estimation. Since $\cos\theta \leq 1$, the bin width in the OMNI method is always greater than or equal to that in ISO-cos at a fixed OSR. This reduces the likelihood of empty bins in edge image projections at larger edge angles. Nonetheless, in scenarios involving smaller angles, the OMNI method's accuracy for sub-pixel oversampling binning does not match that of the ISO-cos method.

Masaoka [25] proposed the OMNI-sine method, an enhancement of the OMNI approach, which adapts the bin width in response to the edge angle. In this method, the sampling interval for each row of the ROI aligns with the bin width at intervals of $\cos\theta$ pixel, and for each column, it aligns at $\tan\theta$ pixel intervals. However, challenges arise when the slanted-edge angle θ approaches 0°, causing the bin width to diminish towards zero and potentially leading to an infinitely large OSR. When the angle is less than 4°, the OSR can exceed 14°. While, theoretically, a higher OSR correlates with greater computational accuracy, practically, an excessively high rate increases computational cost with marginal gains in accuracy. Conversely, a very low rate leads to data underutilization and compromised accuracy, particularly in accurately determining the system MTF at the Nyquist frequency. To mitigate these issues, the bin width is confined within $1/n$ bin to minimize the occurrence of empty bins. The OSR, denoted as ν_{bin}, is defined in Equation (14) and ensures computational efficiency comparable to the ISO method across all angles.

$$\begin{aligned} \theta_{\text{sym}} &= \frac{\arccos(\cos 4\theta)}{4} \\ \nu_{\text{bin}} &= n_{\text{bin}} \cdot 2^{[\log_2(\sin\theta_{\text{sym}})] - \log_2(\sin\theta_{\text{sym}})} \end{aligned} \tag{14}$$

This paper introduces an optimal OSR adaptive model, which is developed by analyzing various ESF processing methods. The model segments the edge angle interval to determine the optimal OSR for each specific angle. The segmentation is as follows: for an edge angle θ in the range [0°, 5.711°), the optimal OSR is set to 5; for θ in [5.711°, 18.435°), it is determined by the cotangent of θ; and for θ in [18.435°, 45°), the optimal OSR is fixed at 3.

In practical applications, optical systems often exhibit aberrations that lead to distortion in edge images, thereby impeding accurate characterization of the ESF distribution in actual images. To maximize the utility of image data while minimizing the influence of random noise, it is essential to reprocess the ESF. This paper describes the application of a fifth-order filter for initial fitting of the ESF, followed by the use of a Savitzky–Golay filter for subsequent smoothing.

2.3. LSF Processing Methods

The ESF can be transformed into the LSF by differentiating it from the discrete ESF. This process occurs post-noise reduction [40], as outlined in Equation (15), where the actual edge distribution overlays the noise interference.

$$\begin{aligned} f'_{ESF}(x) &= f_{ESF}(x) + f_{noise}(x) \\ F\left\{\frac{d}{dx} f'_{ESF}(x)\right\} &= F_{LSF}(j2\pi) + j2\pi F_{noise}(j2\pi) \end{aligned} \tag{15}$$

Due to the spatial domain differentiation of the ESF, noise increasingly impacts the MTF values of the system. The noise coefficient escalates with rising frequencies, indicating a more pronounced noise effect. Therefore, it is necessary to smooth the LSF to mitigate this noise impact. For smoothing, Hamming windows are typically employed. This paper compares the efficacy of the Tukey and Hamming window functions in both time and frequency domains, as depicted in Figure 7.

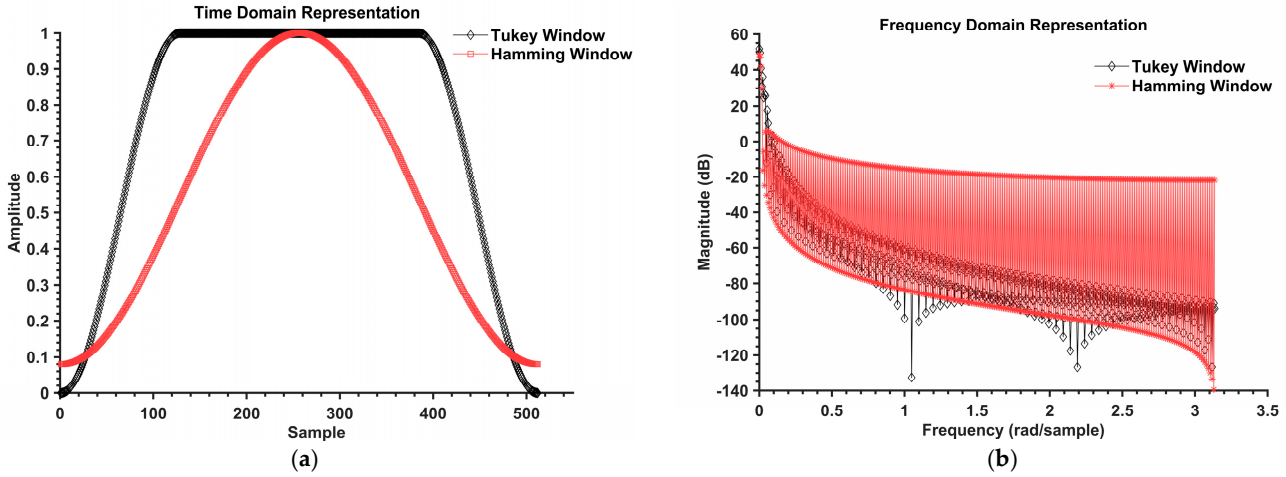

Figure 7. Hamming window and Tukey window frequency and time−domain response curves: (**a**) the time-domain response curve; (**b**) the frequency-domain response curve.

Figure 7 illustrates that in the time domain, the Tukey window (represented by a black line) features smooth transitions at the window's extremities. This characteristic diminishes signal abruptness, thereby aiding in the reduction in spectral leakage. In contrast, the Hamming window (represented by a red line) is generally smoother but exhibits more pronounced jumps at the window's onset and conclusion, potentially leading to increased spectral leakage [41]. In the frequency domain, the Tukey window typically exhibits lower sidelobe magnitudes (peaks outside the main peak) compared to the Hamming window, suggesting enhanced efficacy in minimizing spectral leakage. Moreover, the main sidelobes (central highest peaks) of the Hamming window [42] are marginally wider than those of the Tukey window, indicating a slight inferiority in frequency resolution. These distinctions imply that the Tukey window might be preferable for applications requiring a balance between time–frequency characteristics, reduced spectral leakage, and controlled sidelobe magnitude. Particularly in scenarios demanding precise frequency characteristic measurement or analysis, the Tukey window's attributes may offer superior performance. Therefore, this paper employs the Tukey window for smoothing purposes.

2.4. Processing Steps of the Algorithm Based on the Slanted-Edge Optimal OSR Adaptive Model

According to the comparative analysis of each key link processing method of the slanted-edge method above, the process of the optimal OSR adaptive model based on the slanted edge is shown in Figure 8.

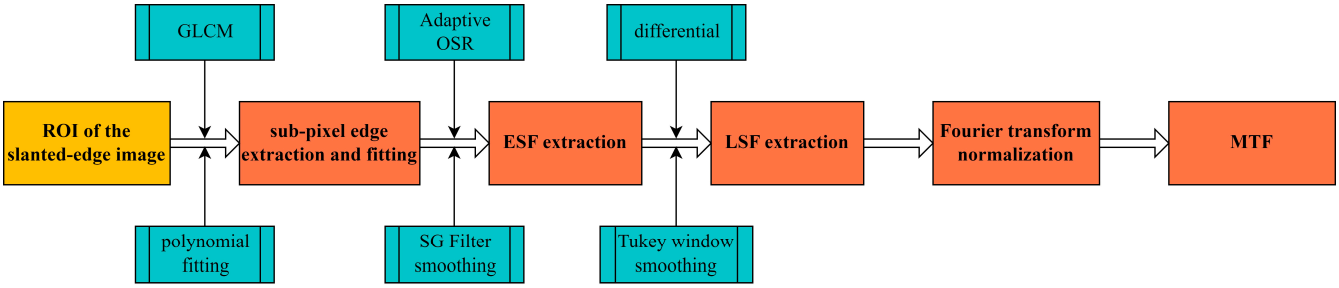

Figure 8. Processing steps of the algorithm in this paper.

2.5. Simulation Experiment Analysis

To precisely assess the accuracy of the algorithm, the RMSE between the test and theoretical MTF curves across various frequencies is utilized as the evaluation metric. This method of accuracy calculation, in contrast to the commonly employed absolute error measurement of MTF values at the Nyquist frequency, encompasses a broader range of

spatial frequencies. It more effectively captures the congruence between the computed and theoretical MTF curves, thereby providing a more comprehensive representation of the algorithm's accuracy.

In line with imaging system theory, the response of an imaging system to spatial frequency can be simulated using a mathematical function, provided the system's parameters are known. These parameters include the aperture diameter D, focal length f, and wavelength λ. Furthermore, Equation (16) defines the cutoff frequency f_{cut} in the context of the diffraction limit.

$$f_{\text{cut}} = \frac{1}{\lambda}\frac{D}{f} \tag{16}$$

The OTF in the diffraction limit can be expressed in Equation (17) as:

$$\text{OTF}_{\text{diff}}(f) = \frac{2}{\pi}\left(\arccos\left(\frac{f}{f_{\text{cut}}}\right) - \frac{f}{f_{\text{cut}}}\sqrt{1-\left(\frac{f}{f_{\text{cut}}}\right)^2}\right) \tag{17}$$

The imaging system's image sensor size is designated as 8 µm, with an aperture diameter of 30 mm, a focal length of 25 mm, and a diffraction wavelength of 10 µm. Utilizing these parameters, the system's OTF is derived in accordance with Equation (17). Subsequently, the PSF is computed through an inverse Fourier transform of the OTF, simulating the system's response to a point light source. The cumulative sum of these PSFs yields the ESF, which represents the system's response to an idealized edge. This ESF is then projected onto a two-dimensional grid, determined by setting the edge angle and the image dimensions (H and V). The ESF effectively models the imaging system's response to the slanted edge, culminating in the generation of slanted-edge images at angles of 5°, 10°, 14°, and 26°, as shown in Figure 9.

(**a**) (**b**) (**c**) (**d**)

Figure 9. Images of slanted edge with different angles: (**a**) slanted-edge angle of 5°; (**b**) slanted-edge angle of 10°; (**c**) slanted-edge angle of 14°; (**d**) slanted-edge angle of 26°.

In this section, edge images are generated using software, after which Gaussian noise with a variance of 0.005 is introduced to the images. Subsequently, the ISO-cos, OMNI-sine, and the adaptive OSR method proposed in this paper are employed to calculate the MTF of the edge images at various angles. Simulations are conducted to validate the accuracy of the algorithm presented in this paper, as illustrated in Figure 10.

Figure 10 clearly demonstrates that the MTF curves calculated using the algorithm proposed in this paper align more closely with the theoretical values compared to the other two methods. Specifically, Figure 10a indicates that the OMNI-sine method is prone to MTF aliasing at high frequencies with slanted-edge angles. Similarly, the ISO-cos method exhibits aliasing in MTF curves at high frequencies when the slanted-edge angle is substantial. The system MTF value at the Nyquist frequency, as depicted in Figure 10d, is 0.1586. Additionally, a comparison of the RMSE between the MTFs and the system values for each method across different frequencies is presented in Table 2.

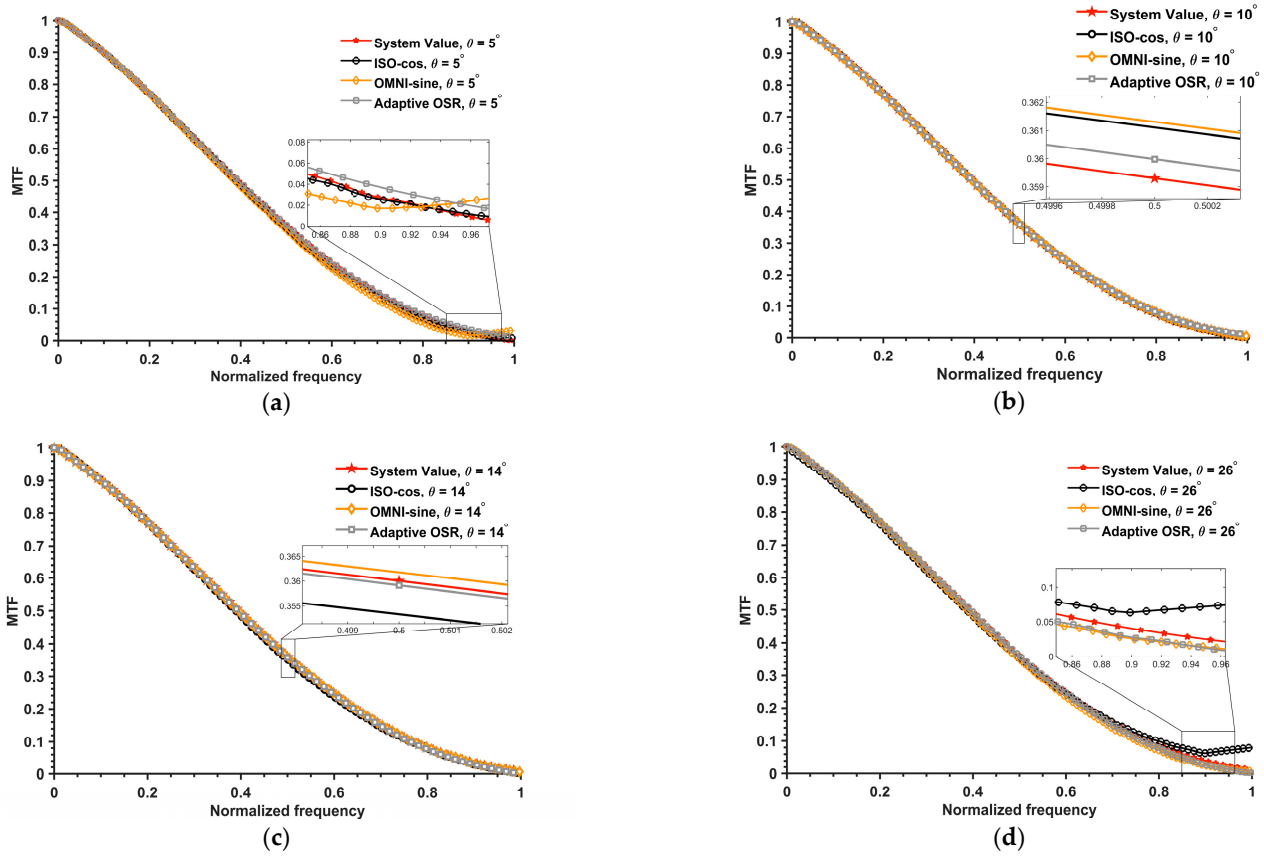

Figure 10. MTF calculation curves at various slanted-edge angles for the three algorithms: (**a**) slanted-edge angle of 5°; (**b**) slanted-edge angle of 10°; (**c**) slanted-edge angle of 14°; (**d**) slanted-edge angle of 26°.

Table 2. RMSE of MTF calculation by different methods.

Angle \ Method	ISO-cos	OMNI-sine	Algorithm in This Paper
5°	0.0495	0.0808	0.0527
10°	0.0301	0.0303	0.0276
14°	0.0337	0.0405	0.0319
26°	0.0905	0.0446	0.0478

It can be seen that the MTF value measured by the algorithm in this paper has the smallest mean square error with the theoretical value, which is closer to the real result.

3. Analysis of Factors Influencing the Results

The slanted edge of the imaging system represents a continuous input signal. When this signal is incident on the image detector element, it remains continuous. However, the sampling process discretizes this continuous signal, transforming it into a step-like distribution on the detector, as illustrated in Figure 11a. This distribution, highlighted by a red circle in the figure, defines the structure known as a "sampling step". The embodiment of the sampling step varies with different tilt angles, requiring different numbers of image lines, as demonstrated in Figure 11b,c.

According to the mathematical relationship, the number of image elements, denoted as y, required to represent a slanted edge with a width of x pixels is given by Equation (18):

$$y \geq x\left[\cot\theta\right] \tag{18}$$

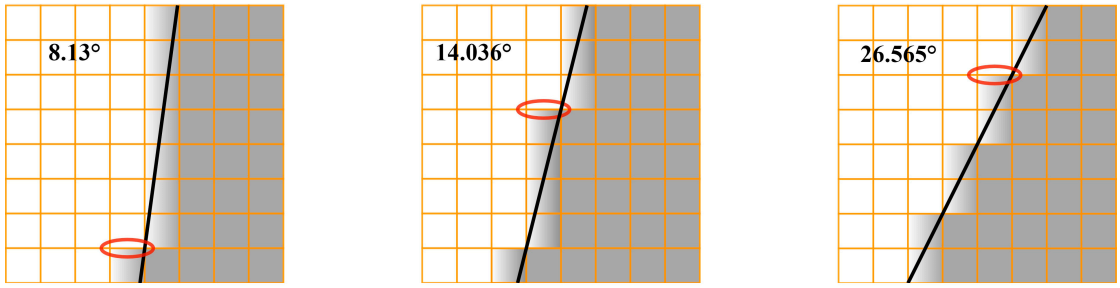

(**a**) (**b**) (**c**)

Figure 11. Schematic diagram of slanted-edge discretization: (**a**) slanted-edge angle of 8.13°; (**b**) slanted-edge angle of 14.036°; (**c**) slanted-edge angle of 26.565°.

Figure 12 depicts the minimum number of pixels along the height of the slanted edge necessary to represent the slanted-edge angle, varying from 1° to 45°, when the width of the slanted edge is fixed at 1 pixel.

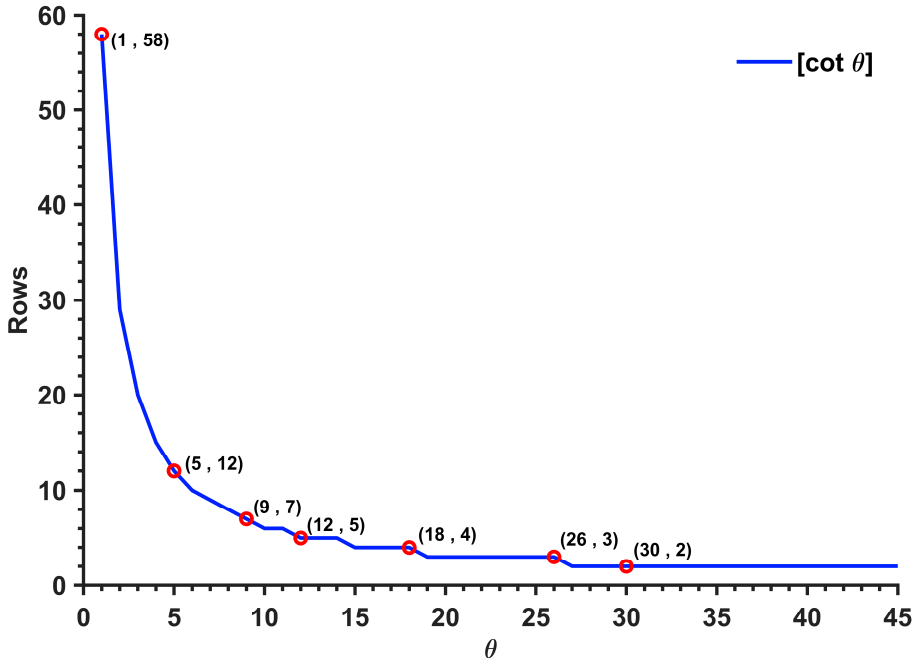

Figure 12. Relationship between slanted-edge angle and number of pixels.

3.1. Effect of Slanted-Edge Angle on Slanted-Edge Method

From Figure 11, it is evident that a smaller slanted-edge angle necessitates a greater number of pixels to represent the angle, leading to an increase in the image size in the height direction of the slanted edge. To explore the impact of the slanted-edge method, particularly how the slanted-edge angle, constrained by the height of the edge, affects the method's results, the imaging process of the imaging system was simulated as per Section 2.4. This simulation involved using a computer to generate 100 × 100-pixel images of a slanted edge with angles increasing from 1° to 45°. The grayscale values for the light and dark areas were set at 255 and 0, respectively. The slanted-edge method was then applied to calculate the MTF of the system at the Nyquist frequency. This paper's analysis includes comparing the results of the proposed algorithm with the theoretical values to evaluate the effectiveness of the slanted-edge method. The comparison of the theoretical and actual calculated values is presented in Figure 12.

Figure 13b demonstrates that the relative error escalates notably when the slanted-edge angle is less than 6°, suggesting that the solution results become highly volatile at

smaller angles. This is attributed to the inadequacy of the actual image's slanted-edge height in fully capturing the nuances of smaller angles. Conversely, when the angle exceeds 12°, the relative error also increases as the angle widens. This rise in error is due to the increased width of the edge under a constant height, which introduces additional noise into the solution results. Therefore, the optimal range for the slanted-edge angle is between 6° and 12°.

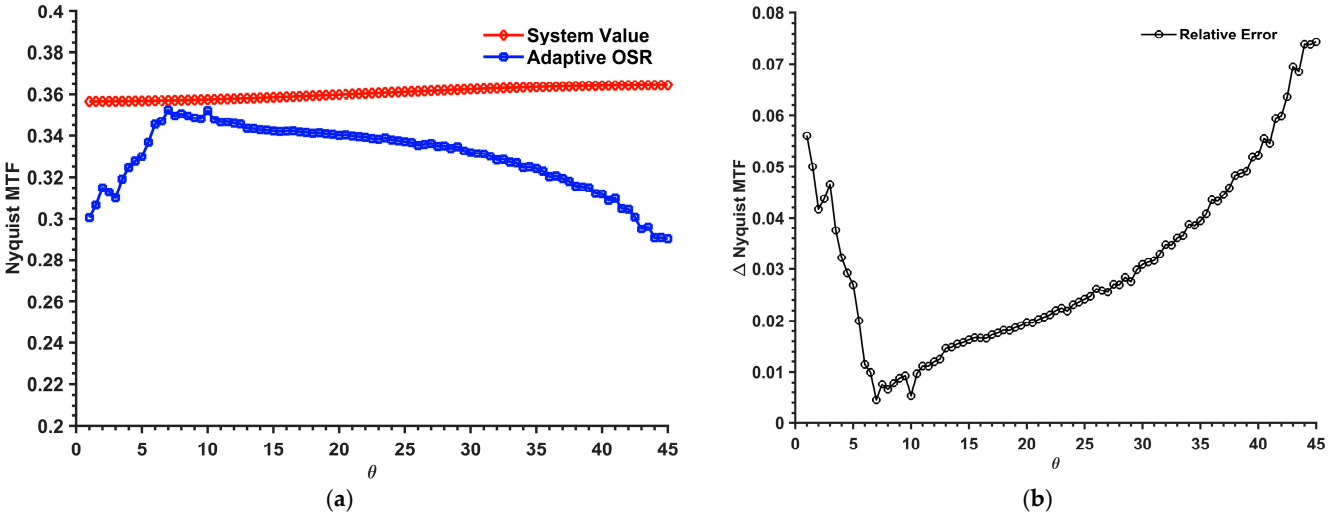

Figure 13. Nyquist MTF for different angles: (**a**) numerical curve at Nyquist frequency; (**b**) relative error curve.

When the slanted-edge angle ranges from 6° to 12°, the relative error between the calculated and theoretical values remains below 0.01. This suggests that within this angle range, the slanted-edge method demonstrates optimal stability, making it the most ideal range for the slanted-edge angle.

3.2. Effect of ROI in Slanted-Edge Images on the Slanted-Edge Method

This section analyzes the impact of slanted-edge height on the slanted-edge method under a specific slanted-edge angle of 7°. Examination of Figure 10 reveals that the continuous signal becomes discretized following the sampling process. Subsequently, the signal's representation on the detector resembles a stair-step distribution. The height of the slanted edge, corresponding to a varying number of steps for a constant angle, introduces result uncertainty. With a slanted-edge angle fixed at 7°, the height fluctuates within a 9-pixel range. Table 3 presents the varied slanted-edge heights for each step. Consequently, simulation experiments were conducted to assess the relationship between slanted-edge height and step distribution.

Table 3. Height of slanted edge for different steps.

Steps	1	2	3	4	5	6	7	8
Rows	2~18	11~27	20~36	29~45	38~54	47~63	56~72	65~81

Figure 14 vividly illustrates the convergence of data, highlighting the correlation between the number of steps in the slanted edge and the precision of experimental results. As the number of steps increases, there is a notable improvement in convergence, with the root-mean-square error remaining below 0.1 when the step count exceeds three. Therefore, an image of the slanted edge should include a minimum of three step structures. Additionally, considering the relationship between the number of slanted-edge steps and their height, as detailed in Table 3, the slanted edge's height within the ROI should be at least 30 pixels for an ideal slanted angle range of $\theta \in [6°, 12°]$.

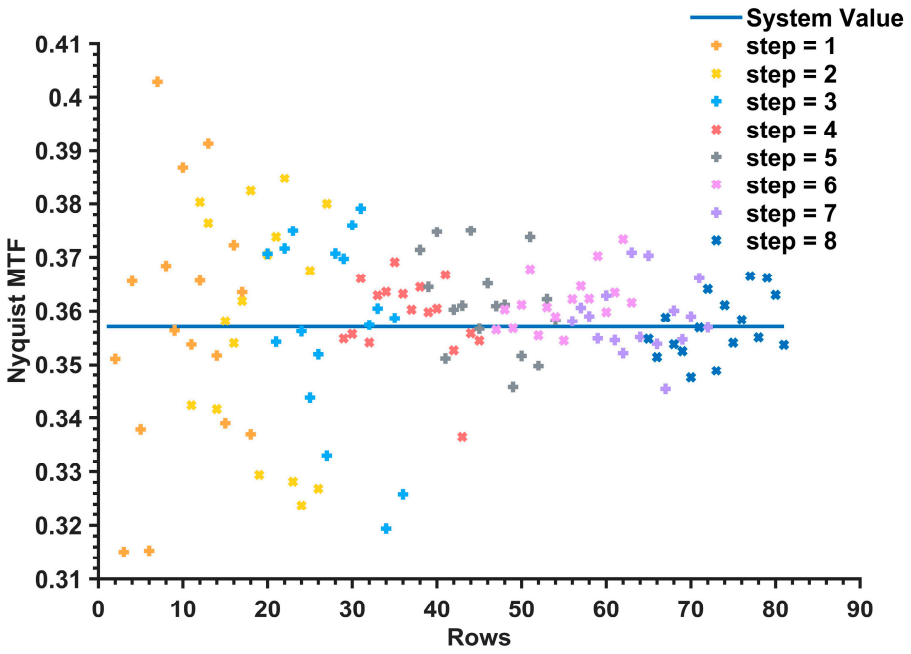

Figure 14. Nyquist MTF versus sampling step curve.

3.3. Effect of Contrast and SNR of Slanted-Edge Images on the Slanted-Edge Method

In this section, we examine the impact of image contrast and SNR on MTF measurements using a slanted-edge angle of 7°. Low edge contrast can hinder the visual distinction of edges, thereby affecting the stability of MTF results. We analyze images with contrasts of 0.95, 0.85, 0.75, 0.66, 0.55, 0.45, 0.35, 0.25, 0.15, and 0.05. Additionally, various noise levels are introduced to these images to achieve slanted-edge images with SNRs of 100, 90, 80, 70, 60, 50, 40, 30, 20, and 10. Using the algorithms proposed in this paper, we explore how image contrast and SNR influence the slanted-edge method. The simulation results are presented in Figure 15.

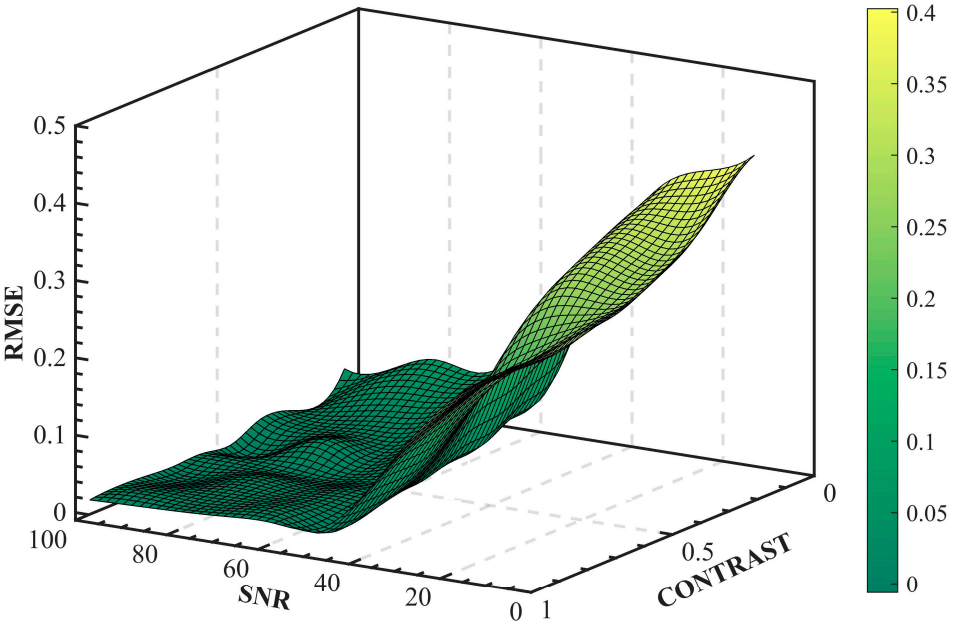

Figure 15. Nyquist MTF at different contrast and SNR.

The presence of noise in the edge image inevitably leads to fluctuations in the MTF curve. As illustrated in Figure 15, random noise significantly impacts MTF calculations. A decrease in the image's SNR results in an increase in the RMSE, leading to a rapid decline in calculation accuracy. Specifically, when the SNR falls below 30 dB, the calculated RMSE of the MTF exceeds 0.2, markedly increasing the likelihood of MTF aliasing. Consequently, the reliability of the measured MTF under these conditions is considerably diminished. In the absence of noise interference, the contrast of the images on either side of the edge marginally affects the accuracy of the MTF calculations. This is evident from Figure 15, which demonstrates that even when the contrast of the gray values on both sides of the edge is reduced to 0.3, the MTF calculation still retains high accuracy. However, as random noise increases, images with higher contrast demonstrate a superior ability to resist noise interference, thereby maintaining higher calculation accuracy.

Consequently, for optimal measurement results, it is essential to maintain an image contrast of at least 0.3 and ensure that the image's SNR exceeds 30.

4. Laboratory Test Results and Analysis

To validate the accuracy and reliability of the testing methodology proposed in this paper, the MTF test experiment was designed for a laboratory CMOS camera, and an experimental verification platform was constructed. This platform comprises an integrating sphere light source, a slanted-edge target, an optical lens, a CMOS camera, a three-dimensional rotary platform, and an image acquisition device. The integrating sphere provides uniform illumination for the slanted-edge target. The light signal, after traversing the optical lens, is captured by the CMOS camera and subsequently converted into a grayscale image through signal acquisition and processing. This image represents the target as captured by the camera's imaging system and is depicted in Figure 16, showcasing the test equipment. The MTF of the optical system under test is computed from the slanted-edge target image using the proposed method. The resulting transfer function values are then employed to evaluate the accuracy and stability of the focal plane position and the MTF values obtained through this test method.

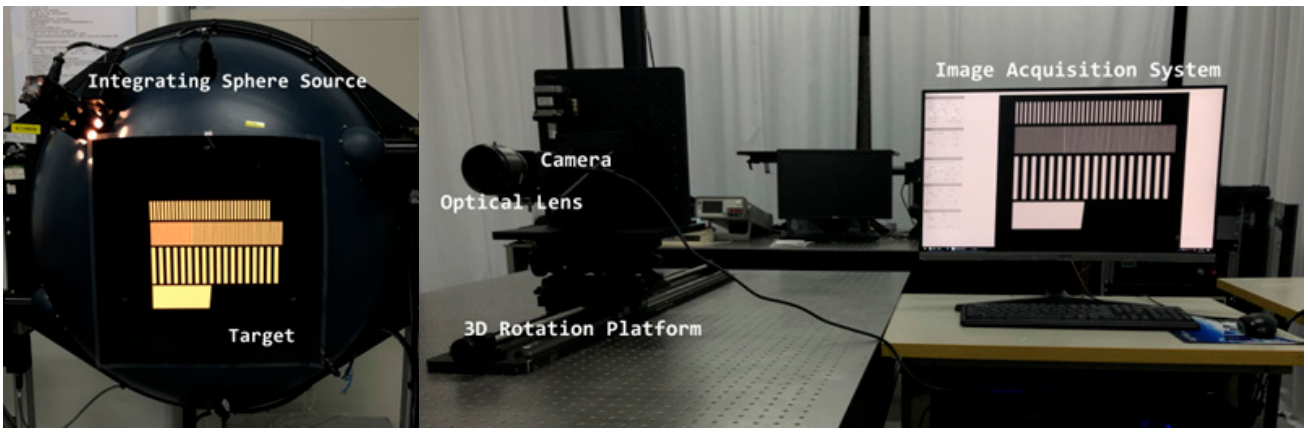

Figure 16. MTF laboratory test system.

The experimental setup included an integrating sphere source, a slanted-edge target, an optical lens, a CMOS camera, a 3D rotation platform, and an image acquisition device, all mounted on an optical vibration isolation platform. The 3D rotation platform was meticulously aligned to ensure the optical path was coaxial, enabling the CMOS camera to fully capture the slanted-edge target image. We maintained a precise 7° angle between the slanted-edge target and the detector. Additionally, the 3D rotation platform facilitated image acquisition at 0.1 mm intervals within a 1 mm depth range beyond the camera's focal length, capturing 20 frames at each position (see Figure 17a). Using the slanted-edge method outlined in this paper, we calculated the MTF values at various positions. These

values were then used to construct through-focus MTF curves, as depicted in Figure 17b. The accuracy of our proposed algorithms was validated against reference MTFs derived from three-bar target images in a controlled laboratory environment.

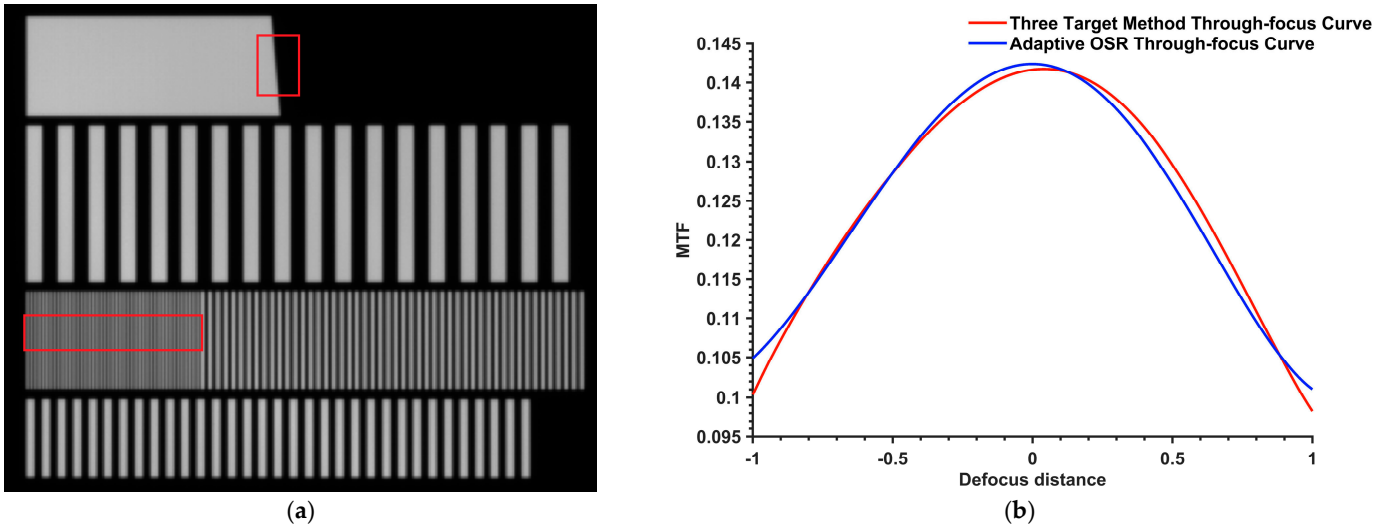

(**a**) (**b**)

Figure 17. Target image and test results: (**a**) target, red rectangular areas are the ROI; (**b**) MTF through−focus curve.

The curve displayed in the figure closely aligns with the through-focus curve derived using the three-bar method. This congruence provides experimental evidence that the slanted-edge method introduced in this paper is a viable approach for calculating the MTF.

Subsequently, we altered the angle between the CMOS camera and the slanted-edge target. The 3D rotary stage was adjusted incrementally, starting from 1°. Slanted-edge target images were captured at every 0.5° increment, collecting 20 frames at each angle, up to a maximum of 45°, as illustrated in Figure 18. This procedure resulted in the acquisition of a total of 1760 slanted-edge target images. To mitigate the effects of air disturbance, the 20 frames obtained at each angle were aggregated and averaged, producing a representative slanted-edge image for each angle. We then computed the MTF values at the Nyquist frequency for the 88 distinct sets of slanted-edge images, facilitating the assessment and analysis of the impact of the slanted-edge angle on the accuracy of the slanted-edge method.

Figure 19 presents the results, illustrating that the trend of MTF values at the Nyquist frequency for various slanted-edge images, as measured in the laboratory, aligns with the simulated results. This alignment corroborates the efficacy of the optimal OSR-based adaptive modeling algorithm introduced in our study. Notably, the MTF relative error remains within 1.5% for slanted-edge angles ranging from 6° to 12°. The stability is particularly pronounced at a 7° slanted-edge angle, suggesting that the slanted-edge algorithm demonstrates optimal stability within this angle range. Additionally, this finding affirms the reliability and precision of the constraints specified in the slanted-edge method proposed in this paper.

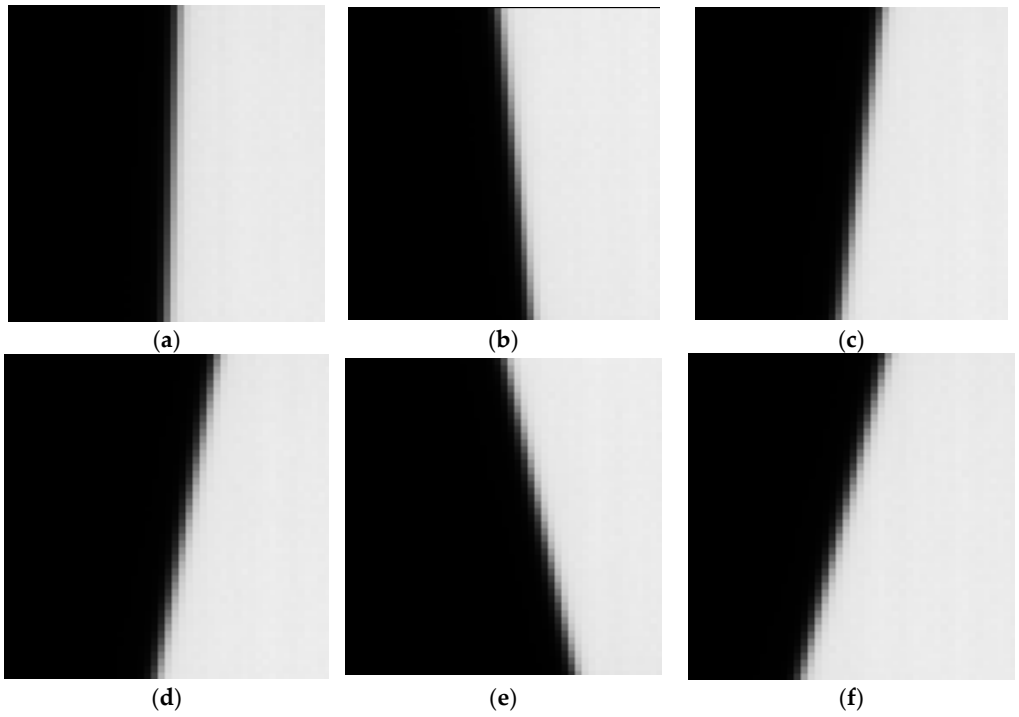

Figure 18. Images of slanted-edge targets at different angles: (**a**) slanted-edge angle of 3°; (**b**) slanted-edge angle of 7°; (**c**) slanted-edge angle of 8°; (**d**) slanted-edge angle of 10°; (**e**) slanted-edge angle of 14°; (**f**) slanted-edge angle of 20°.

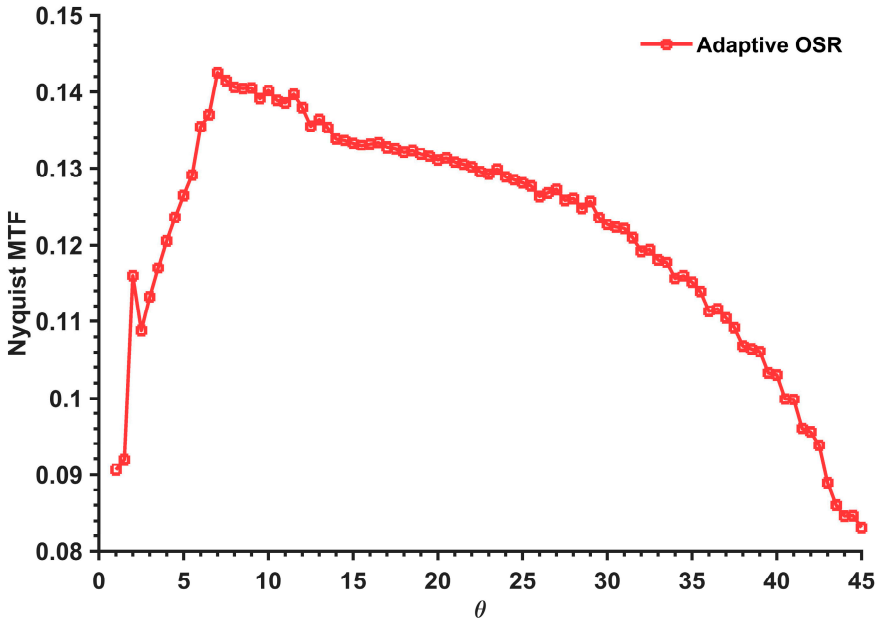

Figure 19. Nyquist MTF at different angles in laboratory testing.

5. Conclusions

In this paper, we address the limitations of existing sub-pixel edge detection and ESF curve extraction algorithms, specifically their low accuracy and high error rates. Through simulation experiments, we generate ideal computer-generated slanted-edge images and introduce varying levels of noise to assess the algorithms' performance. We focus on comparing the accuracy and stability of different methods for calculating the angle in the slanted-edge technique. Furthermore, we examine the impact of the OSR on the method's measurement accuracy and propose an adaptive model based on the optimal OSR. This

model adjusts the sampling rate according to the edge angle, enhancing its applicability across a broader range of angles. Additionally, we employ higher-order polynomial edge fitting to mitigate the effects of spatial aberrations and image noise more effectively.

This paper subsequently analyzes the image factors influencing the slanted-edge method's calculations. Specifically, it analyzes how the slanted-edge angle, ROI, contrast, and SNR impact the method's accuracy. These factors are quantitatively assessed as constraints of the slanted-edge method through simulation experiments. The simulation results show that when the slanted-edge angle is between 6° and 12°, the relative error between the calculated value and the theoretical value is within 0.01, which indicates that when the slanted-edge angle is between 6° and 12°, the slanted-edge method has the best stability in the solving results, and it is a more ideal range of the slanted-edge angle. The ROI of slanted-edge height is at least 30 pixels, and the slanted-edge width is selected based on the principle of including as large a bright and dark area as possible. The SNR of the slanted-edge image significantly influences the results of MTF calculations. As the SNR decreases, there is a rapid decline in calculation accuracy. Conversely, contrast has a minimal impact on MTF calculation accuracy, with results maintaining a high level of precision even when the contrast ratio decreases to 0.3. To ensure optimal calculation results, it is imperative to maintain an SNR greater than 30dB for the slanted-edge image, along with a contrast ratio exceeding 0.3.

At present, the selection of the ROI for slanted-edge images remains a manual process in this paper. Future advancements may involve the integration of neural networks or feature recognition techniques to intelligently automate the selection of the effective ROI. Factors such as atmosphere and motion blur that cause MTF attenuation in photoelectric imaging systems can be added to the subsequent analysis to make it more universally applicable, further improve the algorithm, and increase the computational accuracy. In this paper, we use both simulation and laboratory experiments for algorithm validation and accuracy analysis, which can be followed by on-orbit experiments using real on-orbit image data for further evaluation.

Author Contributions: Conceptualization, J.Y. and Y.Z.; methodology, J.Y.; software, J.Y. and B.Q.; validation, J.Y., X.B. and W.W.; formal analysis, H.L.; data curation, J.Y.; writing—original draft preparation, J.Y.; writing—review and editing, Y.Z., B.Q. and X.B. All authors have read and agreed to the published version of the manuscript.

Funding: This research received no external funding.

Institutional Review Board Statement: Not applicable.

Informed Consent Statement: Not applicable.

Data Availability Statement: Data is contained within the article.

Conflicts of Interest: The authors declare no conflict of interest.

References

1. Kabir, S.; Leigh, L.; Helder, D. Vicarious Methodologies to Assess and Improve the Quality of the Optical Remote Sensing Images: A Critical Review. *Remote Sens.* **2020**, *12*, 4029. [CrossRef]
2. Xu, L.; Yan, C.; Gu, Z.; Li, M.; Li, C. Analysis of Dynamic Modulation Transfer Function for Complex Image Motion. *Appl. Sci.* **2019**, *9*, 5142. [CrossRef]
3. Gu, Y.; Shen, X.; He, G. MTF Estimation via BP Neural Networks and Markov Model for Space Optical Camera. *J. Frankl. Inst. B* **2013**, *350*, 3100–3115. [CrossRef]
4. Boreman, G.D.; Yang, S. Modulation Transfer Function Measurement Using Three- and Four-Bar Targets. *Appl. Opt.* **1995**, *34*, 8050–8052. [CrossRef] [PubMed]
5. Najafi, S.; Madanipour, K. Measurement of the Modulation Transfer Function of a Charge-Coupled Device Array by the Combination of the Self-Imaging Effect and Slanted Edge Method. *Appl. Opt.* **2013**, *52*, 4724–4727. [CrossRef] [PubMed]
6. Kamali-Asl, A.; Sarkar, S.; Shahriari, M.; Agha-Hosseini, H. Slit Slat Collimator Optimization with Respect to MTF. *Appl. Radiat. Isot.* **2005**, *62*, 461–468. [CrossRef] [PubMed]
7. Otón, J.; Sorzano, C.O.S.; Marabini, R.; Pereiro, E.; Carazo, J.M. Measurement of the Modulation Transfer Function of an X-ray Microscope Based on Multiple Fourier Orders Analysis of a Siemens Star. *Opt. Express* **2015**, *23*, 9567–9572. [CrossRef] [PubMed]

8. Sanli, U.T.; Rodgers, G.; Zdora, M.-C.; Qi, P.; Garrevoet, J.; Falch, K.V.; Müller, B.; David, C.; Vila-Comamala, J. Apochromatic X-ray Focusing. *Light Sci. Appl.* **2023**, *12*, 107. [CrossRef]
9. Viallefont-Robinet, F.; Helder, D.; Fraisse, R.; Newbury, A.; van den Bergh, F.; Lee, D.; Saunier, S. Comparison of MTF Measurements Using Edge Method: Towards Reference Data Set. *Opt. Express* **2018**, *26*, 33625. [CrossRef]
10. Nishi, K. Does the Slanted-Edge Method Provide the True Value of Spatial Frequency Response? *J. Opt. Soc. Am. A JOSAA* **2023**, *40*, 259–269. [CrossRef]
11. Ryan, R.; Baldridge, B.; Schowengerdt, R.A.; Choi, T.; Helder, D.L.; Blonski, S. IKONOS Spatial Resolution and Image Interpretability Characterization. *Remote Sens. Environ.* **2003**, *88*, 37–52. [CrossRef]
12. Toutin, T. Comparison of Stereo-Extracted DTM from Different High-Resolution Sensors: SPOT-5, EROS-a, IKONOS-II, and QuickBird. *IEEE Trans. Geosci. Remote Sens.* **2004**, *42*, 2121–2129. [CrossRef]
13. Baraldi, A.; Durieux, L.; Simonetti, D.; Conchedda, G.; Holecz, F.; Blonda, P. Automatic Spectral Rule-Based Preliminary Classification of Radiometrically Calibrated SPOT-4/-5/IRS, AVHRR/MSG, AATSR, IKONOS/QuickBird/OrbView/GeoEye, and DMC/SPOT-1/-2 Imagery—Part II: Classification Accuracy Assessment. *IEEE Trans. Geosci. Remote Sens.* **2010**, *48*, 1326–1354. [CrossRef]
14. Han, L.; Gao, K.; Dou, Z.; Zhu, Z.; Wang, H.; Fu, X. On-Orbit MTF Estimation for GF-4 Satellite Using Spatial Multisampling on a New Target. *IEEE Geosci. Remote Sens. Lett.* **2020**, *17*, 17–21. [CrossRef]
15. Crespi, M.; De Vendictis, L. A Procedure for High Resolution Satellite Imagery Quality Assessment. *Sensors* **2009**, *9*, 3289–3313. [CrossRef] [PubMed]
16. *ISO 12233:2023*; Photography-Electronic Still Picture Imaging-Resolution and Spatial Frequency Responses, Document ISO 12233:2023. Multiple. Distributed through American National Standards Institute (ANSI): Washington, DC, USA, 2023.
17. Kobayashi, S. Nonlinear Model for an Optical Read-Only-Memory Disk Readout Channel Based on an Edge-Spread Function. *Appl. Opt.* **2002**, *41*, 2679–2685. [CrossRef] [PubMed]
18. Li, L.; Cao, J.; Wei, S.; Jiang, Y.; Shen, X. Improved On-Orbit MTF Measurement Method Based on Point Source Arrays. *Remote Sens.* **2023**, *15*, 4028. [CrossRef]
19. Lv, S.; Kemao, Q. Modeling the Measurement Precision of Fringe Projection Profilometry. *Light. Sci. Appl.* **2023**, *12*, 257. [CrossRef]
20. Cho, H.-W.; Yoon, H.-J.; Yoon, J.-C. Analysis of Crack Image Recognition Characteristics in Concrete Structures Depending on the Illumination and Image Acquisition Distance through Outdoor Experiments. *Sensors* **2016**, *16*, 1646. [CrossRef]
21. Masaoka, K.; Yamashita, T.; Nishida, Y.; Sugawara, M. Modified Slanted-Edge Method and Multidirectional Modulation Transfer Function Estimation. *Opt. Express* **2014**, *22*, 6040. [CrossRef]
22. Roland, J.K.M. *A Study of Slanted-Edge MTF Stability and Repeatability*; Larabi, M.-C., Triantaphillidou, S., Eds.; SPIE: San Francisco, CA, USA, 2015; p. 93960L.
23. Tzannes, A.P.; Mooney, J.M. Measurement of the Modulation Transfer Function of Infrared Cameras. *Opt. Eng.* **1995**, *34*, 1808–1817. [CrossRef]
24. Hwang, H.; Choi, Y.-W.; Kwak, S.; Kim, M.; Park, W. MTF Assessment of High Resolution Satellite Images Using ISO 12233 Slanted-Edge Method. In Proceedings of the Image and Signal Processing for Remote Sensing XIV, Cardiff, UK, 15–18 September 2008; SPIE: Bellingham, WA, USA, 2008; Volume 7109, pp. 34–42.
25. Masaoka, K. Edge-Based Modulation Transfer Function Measurement Method Using a Variable Oversampling Ratio. *Opt. Express* **2021**, *29*, 37628. [CrossRef] [PubMed]
26. Burns, P.D.; Williams, D.; Griffith, J.; Hall, H.; Cahall, S. Application of ISO Standard Methods to Optical Design for Image Capture. *Electron. Imaging* **2020**, *2020*, 240–241. [CrossRef]
27. Liu, S.; Liu, K.; Kewei, E.; Wang, T.; Li, Z.; Yao, B. Correction of the Error Induced by Obscurations of Ritchey-Chretien Collimators for High-Resolution Space Camera MTF Measured with the ISO 12233 Slanted-Edge Method. *Optik* **2021**, *235*, 166653. [CrossRef]
28. Wen, G.; Li, S.; Wang, L.; Chen, X.; Sun, Z.; Liang, Y.; Jin, X.; Xing, Y.; Jiu, Y.; Tang, Y.; et al. High-Fidelity Structured Illumination Microscopy by Point-Spread-Function Engineering. *Light Sci. Appl.* **2021**, *10*, 70. [CrossRef]
29. Zhang, Y.; Xian, H. Optical Transfer Function for Incomplete Circular Pupil. *Optik* **2019**, *198*, 162957. [CrossRef]
30. Hu, Z.; Huang, X.; Yang, Z.; Qiu, J.; Song, Z.; Zhang, J.; Dong, G. Reversible 3D Optical Data Storage and Information Encryption in Photo-Modulated Transparent Glass Medium. *Light Sci. Appl.* **2021**, *10*, 140. [CrossRef]
31. Yang, X.; Liang, L.; Li, F.; Tian, Q.; Lu, X.; Xin, L.; Guo, Y.; Dong, W. Hyper-Temporal Data Based Modulation Transfer Functions Compensation for Geostationary Remote Sensing Satellites. *IEEE Trans. Geosci. Remote Sens.* **2022**, *60*, 1–10. [CrossRef]
32. Asnani, S.; Presti, F.L.; Amato, L.; Montrucchio, B. MTFCalculator—A Mobile Application for Measuring the Modulation Transfer Function of Built-in Cameras of Smartphones Using ISO 12233 Slanted-Edge Method. In Proceedings of the 2021 IEEE 6th International Conference on Signal and Image Processing (ICSIP), Nanjing, China, 22–24 October 2021; pp. 1273–1278.
33. Pan, Y.; Cohen, E.; Karimi, E.; Gover, A.; Schönenberger, N.; Chlouba, T.; Wang, K.; Nehemia, S.; Hommelhoff, P.; Kaminer, I.; et al. Weak Measurements and Quantum-to-Classical Transitions in Free Electron–Photon Interactions. *Light Sci. Appl.* **2023**, *12*, 267. [CrossRef]
34. Xiong, J.; Hsiang, E.-L.; He, Z.; Zhan, T.; Wu, S.-T. Augmented Reality and Virtual Reality Displays: Emerging Technologies and Future Perspectives. *Light Sci. Appl.* **2021**, *10*, 216. [CrossRef]
35. Roberti de Siqueira, F.; Robson Schwartz, W.; Pedrini, H. Multi-Scale Gray Level Co-Occurrence Matrices for Texture Description. *Neurocomputing* **2013**, *120*, 336–345. [CrossRef]

36. Gribbon, K.T.; Bailey, D.G. A Novel Approach to Real-Time Bilinear Interpolation. In Proceedings of the DELTA 2004: Second IEEE International Workshop on Electronic Design, Test and Applications, Perth, WA, Australia, 28–30 January 2004; pp. 126–131.
37. Namin, A.H.; Leboeuf, K.; Muscedere, R.; Wu, H.; Ahmadi, M. Efficient Hardware Implementation of the Hyperbolic Tangent Sigmoid Function. In Proceedings of the 2009 IEEE International Symposium on Circuits and Systems, Taipei, Taiwan, 24–27 May 2009; pp. 2117–2120.
38. Chen, H.; Huang, L.; Liu, T.; Ozcan, A. Fourier Imager Network (FIN): A Deep Neural Network for Hologram Reconstruction with Superior External Generalization. *Light Sci. Appl.* **2022**, *11*, 254. [CrossRef] [PubMed]
39. Xie, X.; Fan, H.; Wang, A.; Zou, N.; Zhang, Y. Regularized Slanted-Edge Method for Measuring the Modulation Transfer Function of Imaging Systems. *Appl. Opt.* **2018**, *57*, 6552. [CrossRef] [PubMed]
40. Zhang, S.; Wang, F.; Wu, X.; Gao, K. MTF Measurement by Slanted-Edge Method Based on Improved Zernike Moments. *Senssors* **2023**, *23*, 509. [CrossRef]
41. Burns, P.D.; Masaoka, K.; Parulski, K.; Wueller, D. Updated Camera Spatial Frequency Response for ISO 12233. *Electron. Imaging* **2022**, *34*, IQSP-357. [CrossRef]
42. Bojkovic, Z.S.; Bakmaz, B.M.; Bakmaz, M.R. Hamming Window to the Digital World. *Proc. IEEE* **2017**, *105*, 1185–1190. [CrossRef]